

MPI-AMRVAC: a parallel, grid-adaptive PDE toolkit

Rony Keppens¹

Centre for mathematical Plasma Astrophysics, KU Leuven, Belgium

Jannis Teunissen

CWI, Amsterdam, The Netherlands

Chun Xia

Yunnan University, School of Physics and Astronomy, Kunming, Yunnan, PR China

Oliver Porth

UvA, Amsterdam, The Netherlands

Abstract

We report on the latest additions to our open-source, block-grid adaptive framework MPI-AMRVAC, which is a general toolkit for especially hyperbolic/parabolic partial differential equations (PDEs). Applications traditionally focused on shock-dominated, magnetized plasma dynamics described by either Newtonian or special relativistic (magneto)hydrodynamics, but its versatile design easily extends to different PDE systems. Here, we demonstrate applications covering any-dimensional scalar to system PDEs, with e.g. Korteweg-de Vries solutions generalizing early findings on soliton behaviour, shallow water applications in round or square pools, hydrodynamic convergence tests as well as challenging computational fluid and plasma dynamics applications. The recent addition of a parallel multigrid solver opens up new avenues where also elliptic constraints or stiff source terms play a central role. This is illustrated here by solving several multi-dimensional reaction-diffusion-type equations. We document the minimal requirements for adding a new physics module governed by any nonlinear PDE system, such that it can directly benefit from the code flexibility in combining various temporal and spatial discretisation schemes. Distributed through **GitHub**, MPI-AMRVAC can be used to perform 1D, 1.5D, 2D, 2.5D or 3D simulations in Cartesian, cylindrical or spherical coordinate systems, using parallel domain-decomposition, or exploiting fully dynamic block quadtree-octree grids.

Keywords: adaptive mesh refinement, (magneto)hydrodynamics, PDEs

Email address: rony.keppens@kuleuven.be (Rony Keppens)

URL: perswww.kuleuven.be/Rony_Keppens (Rony Keppens)

¹Corresponding author

1. Introduction

In contemporary astrophysical research, numerical modeling forms a vital ingredient, almost invariably handling strongly nonlinear flows and plasma dynamics (i.e., the fourth and most abundant state of known matter in our universe). Many open source codes [e.g. 1, 2, 3, 4, 5, 6, 7, 8] are actively developed and used, which focus on shock-dominated scenarios in gases or plasmas, enriched by radiative processes, gravitational interactions, as well as various (energy) transport and exchange mechanisms, where the equations of (magneto)hydrodynamics or (M)HD form the core application. These (M)HD equations, covered in various textbooks [e.g. 9], return in many aerodynamical or engineering scenarios. This continuously drives the need for advanced numerical techniques to handle (also transsonic and supersonic) flows about obstacles (airplanes or satellite re-entry problems), ventilation flows through ducts, or the generic behavior of electrically conducting fluids.

Many astrophysical applications must handle a vast range of spatial scales, so it is customary to incorporate adaptivity in the numerical solution, where different strategies exist: dynamically relocating a fixed number of grid points (*r*-refinement, see e.g. [10]); using a dynamic means to increase or decrease the number of grid cells by varying the cell sizes (*h*-refinement); or ensuring that the local polynomial representation of the solution throughout a grid cell employs a differing order (*p*-refinement). Various open source codes [e.g. 2, 3, 4, 7, 11, 12] exploit *h*-refinement, where the mesh has various levels of successively finer grids, organized in a hierarchical manner. We will specify the further discussion to **MPI-AMRVAC**² [13, 8, 14, 11], which evolved from a patch-based adaptive mesh refinement (AMR) framework [15], to a purely block-octree AMR implementation [11, 8].

1.1. **MPI-AMRVAC** code basics

MPI-AMRVAC has been in continued development for more than a decade [15], with modern applications ranging from magnetospheric physics at Earth [16] or in the Jovian system [17], over solar physics challenges [18, 19, 20], to more exotic astrophysical processes such as those encountered in supergiant X-ray binaries [21]. The code has heritage to the original **Versatile Advection Code** (hence **VAC**) [22, 23, 24], which solved (near) conservative sets of mainly hyperbolic partial differential equations (PDEs), and specialized in MHD problems [e.g. 25, 26, 27]. In this paper, we demonstrate that **MPI-AMRVAC** is well suited to handle fairly diverse systems of PDEs, that may even deviate from being advection-dominated problems. Indeed, the modular design makes it easy to introduce PDE systems of the form

$$\partial_t \mathbf{U} + \nabla \cdot \mathbf{F}(\mathbf{U}) = \mathbf{S}(\mathbf{U}, \partial_x \mathbf{U}, \partial_{xx}^2 \mathbf{U}, \dots, \mathbf{x}, t), \quad (1)$$

²<http://amrvac.org>

where the set of variables \mathbf{U} is subject to fluxes \mathbf{F} and source terms \mathbf{S} , where all variables $\mathbf{U} = (U_1, U_2, \dots, U_m)$ are to be solved for their spatiotemporal $U_i(\mathbf{x}, t)$ behavior. The spatial coordinates \mathbf{x} may be 1D, 2D or 3D Cartesian coordinates, or could be polar, cylindrical or spherical in nature.

The HD system in particular has (conservative) variables $\mathbf{U} = (\rho, \rho\mathbf{v}, E)^T$ consisting of density ρ , momentum density vector $\rho\mathbf{v}$ (with velocity \mathbf{v}) and total energy density E (combining kinetic with internal energy in $\rho v^2/2 + p/(\gamma - 1)$ with pressure p and parameter $\gamma > 1$). In the hyperbolic PDE system for HD, the fluxes \mathbf{F} typically split up into an advection $\mathbf{F}_{\text{ad}} \equiv \mathbf{v}\mathbf{U}$ and a non-advective flux \mathbf{F}_{na} , and speed magnitudes $v \equiv |\mathbf{v}|$ may be below, equal or above the local physical sound speed. In MHD, also the magnetic field vector \mathbf{B} enters as a variable. To handle discontinuous, shocked flow problems in (M)HD, it is imperative to use conservative numerical schemes [e.g. 28, 29, 9], which usually handle fluxes \mathbf{F} in a manner exploiting the (approximate) solution of local Riemann problems (i.e., initial conditions separating two constant states \mathbf{U}_l and \mathbf{U}_r , to the left and right of the discontinuity, respectively). For both the HD and the MHD equation set, in their Newtonian as well as special relativistic variant [30, 11], codes like MPI-AMRVAC offer a wide variety of spatio-temporal discretizations, to advance initial conditions augmented with boundary prescriptions, in 1D, 2D or 3D configurations. For MPI-AMRVAC, the **Fortran** source code is documented at amrvac.org, and available on [GitHub](https://github.com). Making use of [Doxygen](http://www.doxygen.nl)³, the inline documentation is automatically turned into dependency graphs, flow charts, and searchable source code, which is updated daily to reflect the current status of the code development.

1.2. Adding a new PDE system

Any system of the form given by Eq. (1) may be added to the framework, whose source code is typically located in `amrvac/src` (and an environment variable `AMRVAC_DIR` is to be set to locate this `amrvac` directory). The minimal requirement for adding a new system is to create a corresponding system module (a subdirectory `amrvac/src/newsystem`) quantifying the variables \mathbf{U} , fluxes \mathbf{F} and source terms \mathbf{S} . In the generic physics module `amrvac/src/physics/mod_physics.t`, procedure pointers are initialized and their calling interface is predefined, for use in the PDE systems to implement. Among other procedures, this generic module contains `phys_get_flux` and `phys_add_source` interfaces, which must be fully provided in the module `amrvac/src/newsystem/mod_newsystem_phys.t` of a newly added system. For example, the available (M)HD systems are found in `amrvac/src/hd` and `amrvac/src/mhd`, where the system-specific initializations are handled by an `mod_hd.t` and `mod_mhd.t` activation module, while the actual equations (variable definitions, fluxes, sources and corresponding time step constraints) are to be found in `mod_hd_phys.t` and `mod_mhd_phys.t`. Besides the mentioned interfaces for providing fluxes and sources, other procedures of interest are

³<http://www.doxygen.nl>

- `phys_add_source_geom` for the handling of geometric source terms, needed when solving the same system in polar, cylindrical or spherical coordinates;
- `phys_get_v_idim` to specify an advection velocity in the `idim` direction, when an advective flux \mathbf{F}_{ad} is to be used. Note that this direction refers to x , y or z in Cartesian cases, while it is e.g. r , φ in a polar grid;
- `phys_get_dt` to provide a system-specific time step constraint, that would be in addition to the usual Courant-Friedrichs-Lewy (CFL) limit for explicit time stepping schemes;
- `phys_get_cmax` and `phys_get_cbounds` to quantify the maximal physical propagation speed and any minimal and maximal bound on that speed, useful for computing the CFL timestep limit, or in use for the simplest of any approximate Riemann solver methods (i.e. the local Lax-Friedrich or TVD-LF method [31, 23], as well as its HLL extension [32], which are used heavily in (M)HD applications).

If the system of equations differentiates between conservative \mathbf{U} and primitive variables \mathbf{V} , like the set $\mathbf{V} = (\rho, \mathbf{v}, p)^T$ with pressure p for the set of $\mathbf{U} = (\rho, \rho\mathbf{v}, E)$ in HD, one can provide conversion formulae from conservative to primitive in the procedure `phys_to_primitive`, while its reverse `phys_to_conserved` switches primitive variables back to conservative ones. To benefit optimally from the dimension-independent implementation of our code, these routines best exploit the **LASY** syntax [33], which means writing the coordinate array \mathbf{x} as

```
x(ixI^S,1:^ND)
```

which will expand the segment [^]S when the dimensionality $\text{[^]ND}=2$ to

```
x(ixImin1:ixImax1,ixImin2:ixImax2,1:2)
```

1.3. Adaptive mesh refinement and parallelization

When implementing a new system in **MPI-AMRVAC** according to the procedure just explained, one can directly benefit from its dimension-independent way to solve the system (1) with a variety of time stepping schemes, splitting strategies for handling sources, and exploit its parallel implementation to run efficiently on laptops to the most modern supercomputers. The **Message Passing Interface** or **MPI** based parallelization can always exploit a domain-decomposition by specifying block sizes that equally divide up the computational domain (e.g., one may decide to use a 200×200 2D mesh, divided into 400 blocks of size 10×10). The AMR stands for Adaptive Mesh Refinement, where one relies on a block-based quadtree-octree (in 2D-3D) means of hierarchically adjusting the computational mesh to the evolving solution. The blocksize can be specified and adjusted by the user. A fair variety of automated as well as user-specific means to set (de)refine criteria is available, and they work for all dimensionalities and coordinate systems provided. The excellent scaling of the parallel

implementation has been demonstrated in previous work [14], while the specification of a new system of equations is essentially devoid of any MPI procedures, except for trivial `mpistop('error_message')` interfaces to `MPI_ABORT` calls for catching erroneous input parameter specifications.

The AMR strategy operates as follows. The user specifies a block size `block_nx1`, `block_nx2`, ... for each dimension of the problem at hand, and a conforming domain size in number of grid cells `domain_nx1`, `domain_nx2`, ... at the lowest resolution. The actual domain physical extent is specified by coordinate pairs, such as `xprobin1`, `xprobmax1` for the minimal and maximal x -coordinate, respectively. A maximal number of refinement levels is set through `refine_max_level`, and actual adaptive runs imply that this maximal refinement level is ≥ 2 , while a unit value realizes a pure domain-decomposition computation. When adaptivity is turned on, all blocks at grid levels below `refine_max_level` evaluate a user-selected refinement criterion in every grid cell. The default refinement criterion is a Lohner type estimator [34], where we essentially quantify local weighted second derivatives (for details, see [11]), and this for a user-selected set of variables. This then provides an error in all grid cells of the evaluated blocks. A block is then refined using a fixed refinement ratio of 2 (in 2D this implies splitting the block in 4, in 3D each block creates 8 children blocks) as soon as it has a single point whose error exceeds a user-set tolerance. For a block to be coarsened, all its cells must have the error below a user-set fraction of the previous tolerance. Our implementation also allows the user to intervene with the automated refinement, either overruling or enforcing refinement when necessary.

In this paper, some exemplary problems are presented, where our flexible means of post-processing multi-dimensional data is exploited. The latter comprises possibilities to convert data files on the fly (or after the computation is completed) to data formats directly importable in open-source visualization software like `Paraview`⁴ or `VisIt`⁵. Alternatively, one may use the many provided `python` scripts to e.g. regrid the hierarchically meshed data to a uniform coverage, and use free plotting packages.

1.4. Multigrid functionality

The idealized (M)HD systems which feature in many astrophysical applications are hyperbolic in nature, but when effects like thermal conduction, viscosity, or resistivity are incorporated, parabolic source terms appear. Typical diffusion terms may well render the standard explicit time stepping strategies impractical, as then the time step constraint scales with $\Delta t \propto h^2$, for grid spacing h , prohibiting the use of ultra-high resolution. This is in direct conflict with the usual advantage offered by an AMR code, allowing for extreme resolutions at affordable costs. To alleviate this drawback, a recent extension of our code is its coupling to a fast elliptic solver [13]. The block-adaptive grid used in

⁴<https://www.paraview.org>

⁵<https://wci.llnl.gov/simulation/computer-codes/visit>

MPI-AMRVAC suggests the use of a (geometric) multigrid strategy, where Poisson or Helmholtz equations, with variable coefficients, can be solved in a highly scalable fashion. This recent addition is e.g. useful for handling the Maxwell equation $\nabla \cdot \mathbf{B} = 0$ in multi-dimensional MHD problems, but may also be used to implement particular implicit-explicit (IMEX) discretizations of PDEs containing stiff sources (as demonstrated further on), to handle any typical parabolic terms, to implement incompressible (M)HD equations, or to solve astrophysical applications involving self-gravity. In the next section, we include cases where the multigrid functionality proves helpful to efficiently compute PDE solutions.

2. Example applications

2.1. Korteweg-de Vries computations

As a first demonstration, we present 1D and 2D solutions for a nonlinear scalar equation known as the Korteweg-de Vries equation. This equation combines nonlinear advection with a source term containing a third-order derivative,

$$\partial_t \rho + \nabla \cdot \left(\frac{1}{2} \rho^2 \mathbf{e} \right) = -\delta^2 \sum_{i=1}^D \partial_{xx_i} \rho, \quad (2)$$

where $\mathbf{e} = \sum_{i=1}^D \hat{\mathbf{e}}_i$ in a D -dimensional setup, with Cartesian unit vectors $\hat{\mathbf{e}}_i$. In 1D, this recovers the original Korteweg-de Vries or KdV equation

$$\partial_t \rho + \rho \partial_x \rho + \delta^2 \partial_{xxx} \rho = 0, \quad (3)$$

where δ is a fixed parameter. For $\delta = 0$, we get the nonlinear Burgers equation, which can be used to test shock formation through wave steepening and its numerical realization [35]. In [36], the 1D KdV equation (3) was solved numerically on a periodic domain $x \in [0, 2]$, with $\delta = 0.022$, and initial condition provided by $\rho(x, t = 0) = \cos(\pi x)$. This classic paper [36] documented how the numerical solution showed the spontaneous development and interaction of multiple solitons, where the nonlinear term causing wave steepening is balanced by the dispersive source term to maintain their integrity.

In MPI-AMRVAC, the scalar Eq. (2) is implemented in a `amrvac/src/nonlinear` module, and a Boolean `kdv_source_term` can activate the addition of the dispersive source term. This source term can be evaluated using a fourth order central difference evaluation, requiring three ghost cells to each block when a domain-decomposition strategy is used. We solved the KdV equation on a time interval $t \in [0, 5]$, using 600 grid points, subdivided into 10-cell blocks. This test was run without AMR. A Courant number of 0.9 is used for the CFL condition, where the local absolute value of the scalar ρ sets the maximal signal speed. An additional time step limit is enforcing $\Delta t \leq 0.9(\Delta x)^3/(3\sqrt{3}\delta^2/2)$, where we follow a prescription specified by [37]. For the handling of fluxes, we use a conservative finite difference scheme using a fifth-order, monotonicity preserving MP5 reconstruction [for details, see 14, and references therein]. The

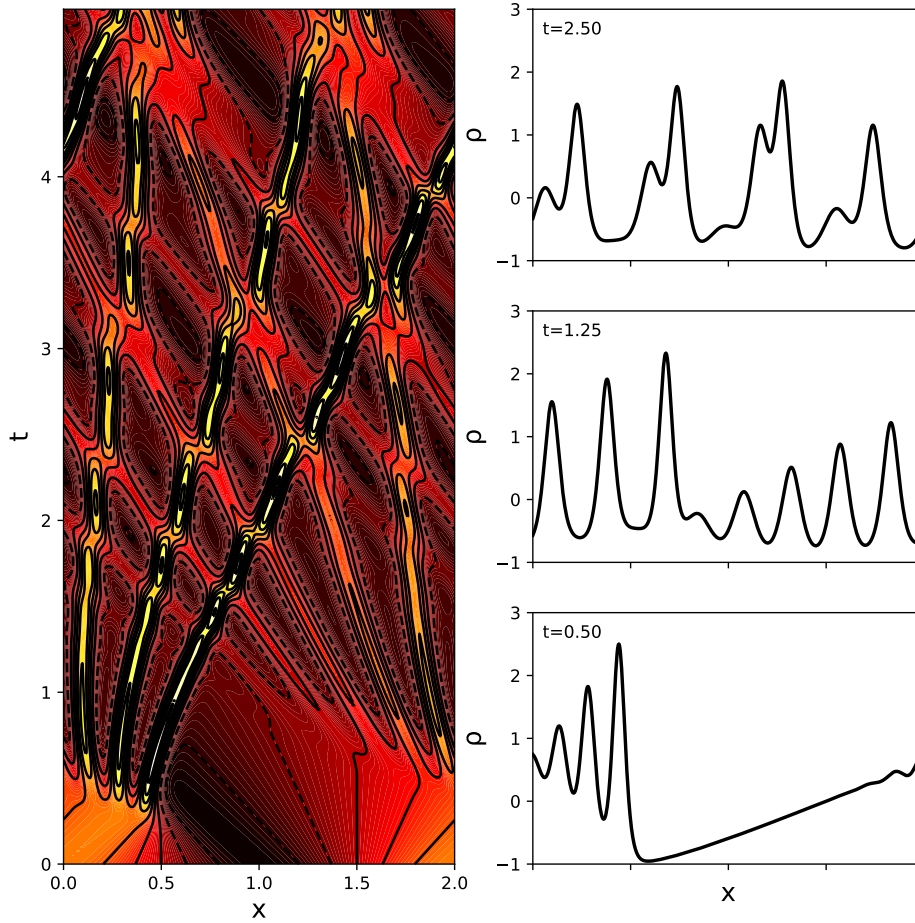


Figure 1: A 1D KdV simulation, showing $\rho(x, t)$ at left in a contour view, with selected $\rho(x)$ variations obtained at the times indicated.

combination of the conservative finite difference scheme, a three-step Runge-Kutta time integrator, and the central difference source evaluation, makes that the numerical solution conserves $\int_0^2 \rho dx$ exactly, which is a known property of the KdV equation. In Fig. 1, we show the solution $\rho(x, t)$ in a contour plot view on the left, where one recognizes how the original cosine variation leads to three sharply peaked solitons that eventually travel forward through the domain, while five weaker backward propagating solitons emerge somewhat later. Their repeated interactions as they pass periodically across the boundaries are very well represented. At right in Fig. 1, selected instantaneous $\rho(x)$ profiles at times $t = 0.5, 1.25$ and 2.5 are provided.

As stated, any multi-dimensional variant of Eq. (2) can now easily be simulated as well, and we compare 2D solutions for a Burgers equation (where $\delta = 0$) to the 2D version of the previous KdV test ($\delta = 0.022$). The double periodic do-

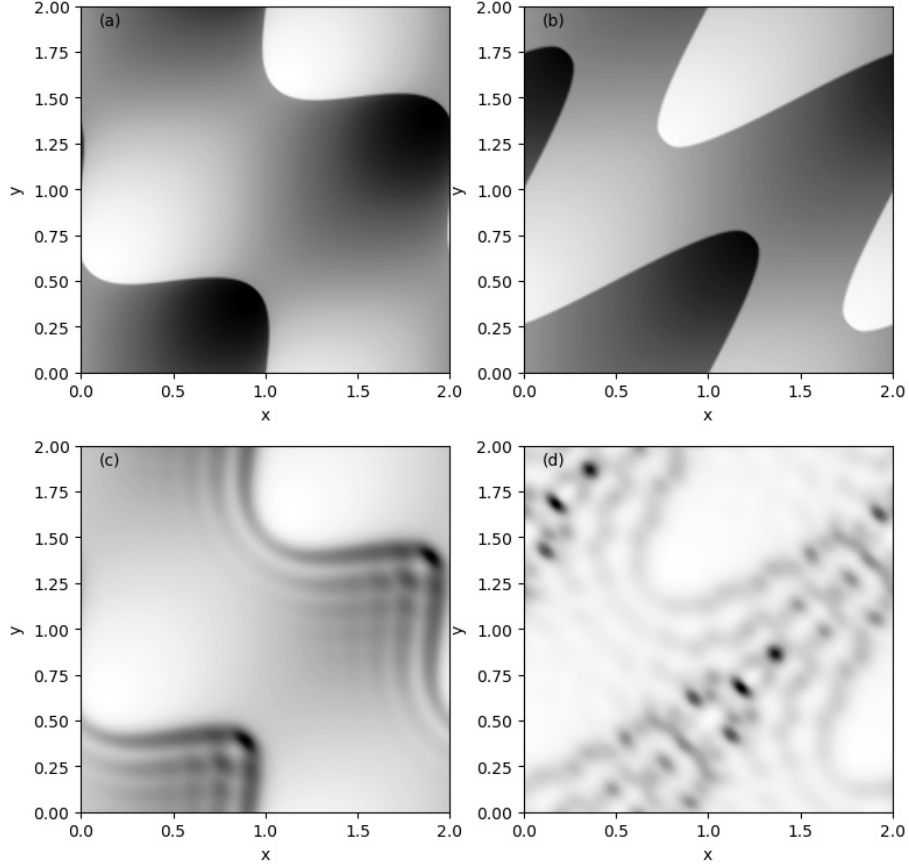


Figure 2: Instantaneous solutions at $t = 0.4$ (left panels (a) and (c)) and $t = 1$ (right panels (b) and (d)), comparing Burgers (top (a) and (b)) with KdV (bottom (c) and (d)).

main $[0, 2] \times [0, 2]$ is initialized with $\rho(x, y) = \cos(\pi x) \sin(\pi y)$, using a 200×200 grid in blocks of 10×10 , again in domain-decomposition mode without AMR for simplicity, since the computational cost for solving a single scalar equation is rather small. We use the same scheme combination as before, only reducing the source-related time step limit to $\Delta t \leq 0.4(\Delta x)^3/(3\sqrt{3}\delta^2/2)$. In Fig. 2, snapshots of the density profile at $t = 0.4$ (left column) and $t = 1$ (right column) are compared for the Burgers equation (top row) versus the KdV system (bottom row). Note the clear shock-dominated solution for the 2D Burgers variant, while the KdV equation again shows soliton-like features developing spontaneously. The patterns observed in the KdV solutions remind us of ripples in (shallow) water and their interactions. This is not surprising, since the original KdV equation arose from analyzing a specific limit of the shallow water equations, to which we turn attention next.

2.2. Shallow water test problems

The shallow water equations can be formulated as

$$\partial_t \begin{pmatrix} h \\ h\mathbf{v} \end{pmatrix} + \nabla \cdot \begin{pmatrix} \mathbf{v}h \\ \mathbf{v}\mathbf{v}h + \frac{1}{2}h^2\mathbf{I} \end{pmatrix} = \mathbf{S}, \quad (4)$$

where one solves for the height profile $h(x, y, t)$ with (height-averaged) speeds $\mathbf{v} = (v_x(x, y, t), v_y(x, y, t))$ affected by gravity. \mathbf{I} is the unit tensor. The above formulation exploits a dimensionless form of the shallow water equations, where lengths are scaled as $\bar{h} = h/a$ and times $\bar{t} = t\sqrt{g/a}$, where a is a reference length unit (e.g. a can be set to 1 meter) and Earth's gravitational acceleration is $g = 9.8 \text{ m/s}^2$. Eq. (4) is to be read with $h \rightarrow \bar{h}$ and similarly for all quantities, while the source term \mathbf{S} may introduce resistance to the flow and bottom topology [38, 39]. The shallow water equations make sense in 2D, and they can be solved on either a Cartesian domain, or a polar (r, φ) grid. The latter introduces geometric source terms, in particular a source $(\frac{1}{2}h^2 + hv_\varphi^2)/r$ for the radial momentum hv_r , as well as a term $-hv_rv_\varphi/r$ for the azimuthal component hv_φ . These geometric source terms are then in addition to possible resistance or flow bed topology terms encoded in \mathbf{S} .

In MPI-AMRVAC, the above equation set is in fact available within the HD module, where one recognizes the fact that system (4) is identical to the subset of mass and momentum conservation laws in the Euler equations, with the ‘pressure’ given by $h^2/2$. Hence, a switch to avoid using an energy variable E is introduced in our `amrvac/src/hd` system, in which case the ‘pressure’ $p = c_{\text{ad}}\rho^\gamma$, where a polytropic relation between density ρ and pressure introduces two free parameters, c_{ad} and γ . The ‘sound’ signal speed (squared) is then $c^2 = \gamma c_{\text{ad}}\rho^{\gamma-1}$, and the shallow water system arises for the identification $\rho \equiv h$, $c_{\text{ad}} = 0.5$ and $\gamma = 2$. In fact, our HD system module has various switches for handling either subcases of the full Euler system (or Navier-Stokes when activating viscosity), or extensions of the Euler system where additional ‘dust’ species are handled as pressureless fluids, coupled to the Euler gas by means of drag terms [14, 40]. Hence, a particular equation module can serve multiple purposes.

As a stringent test of the shallow water implementation, we target the reference test introduced by [41] and discussed in [38], mimicking a circular dam break where there are no extra source terms \mathbf{S} . The test is in fact a 1D Riemann problem in a cylindrical configuration, having water height $h_{\text{in}} = 2.5 \text{ m}$ inside a circular dam of radius $r_{\text{dam}} = 2.5 \text{ m}$, while the exterior has a water height of $h_{\text{ext}} = 0.5 \text{ m}$. We choose to solve this problem twice, once on a 2D polar grid on a disk of radius 20 meters, and once in a 2D Cartesian domain of size $40 \text{ m} \times 40 \text{ m}$. The solutions must obviously agree, but the latter one could suffer from artificial deformations when solving an azimuthally symmetric problem on a square grid. In this problem, we use AMR and exploit a total of 3 refinement levels in both the polar and the Cartesian setup.

In Fig. 3, we show at right the solution at dimensionless time $t = 15$ (physical time $t = 4.79 \text{ s}$), as a contour plot of the $h(r, \varphi)$ solution. At left, the

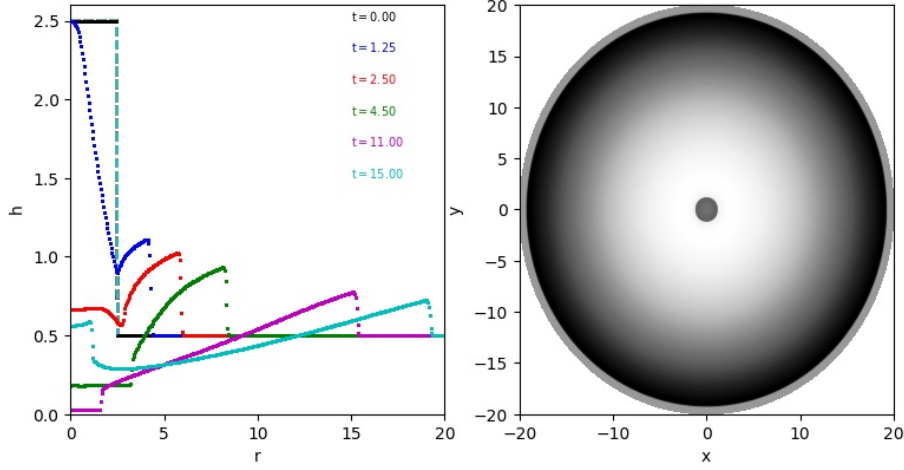


Figure 3: A circular dam break problem, solved on a polar adaptive grid. Left: scatter plots of $h(r)$ at selected times. Right: contour plot of $h(r, \varphi)$ at $t = 15$.

same solution, as well as several earlier snapshots (between $t = 0$ and $t = 15$) are plotted as a scatter plot where all gridcells are visualized. The symmetry (i.e. the 1D nature of this problem) is perfectly preserved, as each dot in the scatter plot is simply repeated for as many azimuthal grid cells as used. We actually adopted a base grid level of 100×100 in (r, φ) , augmented with two additional refinement levels, triggered on height and momentum variations, effectively showing a 400×400 resolution. Block sizes of 10×10 are used, and the boundary conditions use a π -periodic treatment across the $r = 0$ pole [42], periodicity in φ , and a zero gradient (Neumann) extrapolation at $r = 20$. As spatio-temporal integration method, we combined an HLL scheme [32], a three-step Runge-Kutta, and a Koren limiter [43] based reconstruction procedure, with a Courant number of 0.9.

The same problem, now solved on a Cartesian grid, under otherwise identical settings (except for adjusting the domain and the boundary condition on the y -borders), is displayed in the same fashion in Fig. 4. Note how the contour plot at $t = 15$ is visually indistinguishable from its polar variant, while the Cartesian grid now obviously samples the radial profile more frequently when plotted as a scatter plot of $h(r)$ (left panel). For both the polar and Cartesian realization, the AMR that originally locates at the initial discontinuity essentially spreads across the full domain, capturing the outward propagating shock front and the rapid central height variation within $r \leq 5$ as seen in the left panels of both figures.

2.3. Hydrodynamical tests

In this section, we show two example tests for the HD system, where now the equation for the energy density variable $E = \rho v^2/2 + p/(\gamma - 1)$ is included.

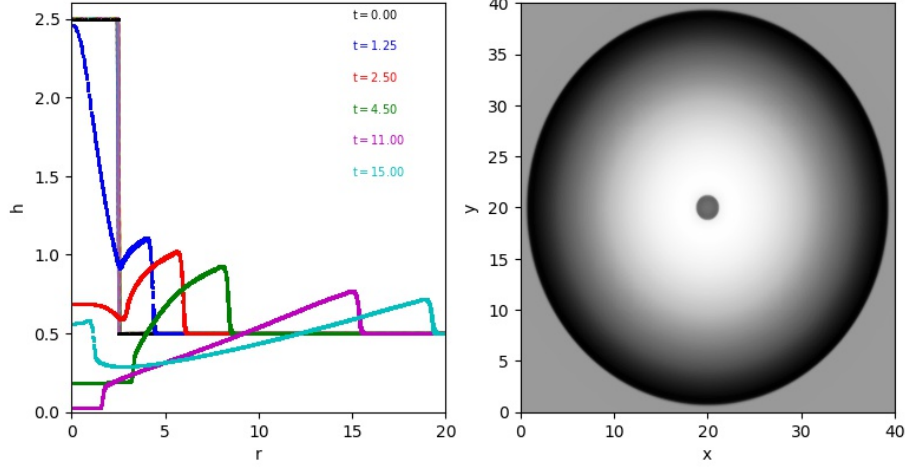


Figure 4: The same as Fig. 3, but now solved on an adaptive Cartesian grid.

We set $\gamma = 5/3$, the standard value for an ideal monoatomic gas. In the first test, a convergence study of an Euler solution is made on uniform grids, while the second test shows solutions for the compressible Navier-Stokes system, using AMR in combination with embedded boundaries.

2.3.1. Gresho-Chan vortex

In the astrophysics literature, one finds many implementations of the HD system which exploit Smooth Particle Hydrodynamics (or SPH) techniques. These are meshless treatments of the governing conservation laws, and are in common use for large-scale cosmological simulations. A frequent test for any novel SPH variant, or for general new HD codes [e.g. 44, 45, 46, 47], is the so-called Gresho-Chan vortex [48], which is believed to be a stationary solution to the Euler system where a pressure gradient balances the centrifugal force of a rotating gas. The initial condition generally has the form

$$p = \begin{cases} \frac{1}{\gamma M^2} + 12.5r^2 & 0 \leq r < 0.2 \\ \frac{1}{\gamma M^2} + 12.5r^2 + 4(1 - 5r - \ln(0.2) + \ln(r)) & 0.2 < r \leq 0.4 \\ \frac{1}{\gamma M^2} - 2 + 4\ln(2) & r > 0.4 \end{cases}, \quad (5)$$

for the pressure, while the rotation velocity is simply

$$v_\varphi = \begin{cases} 5r & 0 \leq r < 0.2 \\ 2 - 5r & 0.2 < r \leq 0.4 \\ 0 & r > 0.4 \end{cases}. \quad (6)$$

A uniform density $\rho = 1$ completes the setup, where the Mach number M can be varied, a typical value is $M = 0.34641 = \sqrt{3}/5$. We use a square domain $[-0.5, 0.5] \times [-0.5, 0.5]$, translating the flow setup to v_x and v_y velocities,

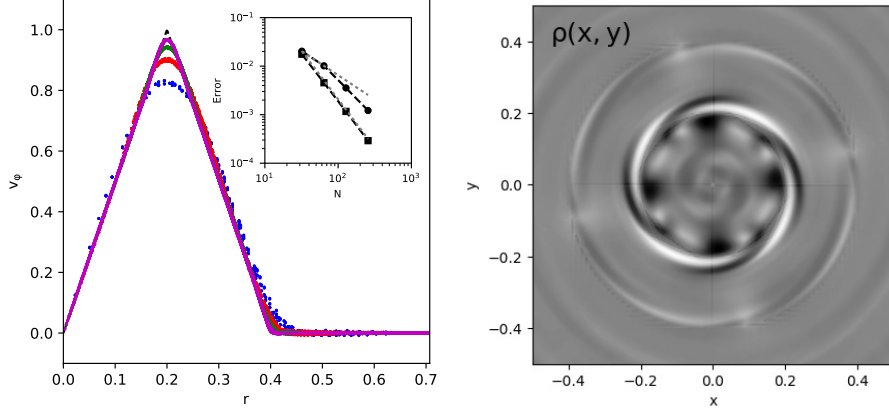


Figure 5: The azimuthal velocity profile (left panel) for the Gresho-Chan vortex test, at increasing resolutions, in a scatter plot from the Cartesian 2D data. The inset quantifies the 1-norm for the rotation profile deviation (solid circles) and the 2-norm error in the pressure profile (squares) and we find better than 1st and up to second order convergence. The right panel shows the density distribution at time $t = 2$. The variation in density is minute (order $1/10000$), but a physically meaningful pattern emerges, indicating the liability of this equilibrium to a linear instability.

and use a one-step high-order TVD method with a Monotonized Central (or ‘woodward’) limiter [23]. This scheme exploits the full approximate Roe solver that is aware of the characteristic decomposition in its flux computation. We solve up to $t = 2$, with a Courant number of 0.9. This problem is solved on uniform meshes (no AMR), of size 32×32 , 64×64 , 128×128 and 256×256 , respectively (our block size is always 8×8) to demonstrate proper convergence. Info on the solution obtained is in Fig. 5, where the left panel shows a scatter plot of the radial profile of $v_\phi(r)$ (similar to the Cartesian version of our dam break problem in Fig. 4), this time for all the mesh sizes exploited. One can see that the azimuthal velocity nicely converges to the analytic initial condition, and the convergence behavior is quantified in the inset in the left panel, where the 1-norm of the error in the obtained azimuthal velocity profile is shown with circular symbols, while the 2-norm for the error in the pressure profile is shown with squares. To guide the eye, dotted lines indicating first as well as second order convergence are also provided. One observes that the pressure profile converges with second order accuracy, while the azimuthal velocity also behaves better than 1st order as soon as sufficient grid points are exploited (the 32×32 run has roughly 12 grid points through the disk radius). Modern SPH variants demonstrate typically a $N^{-0.8}$ convergence rate in 1-norm [45], where N is then the equivalent 1D grid size, and hence only reveal sublinear convergence.

At right, the density profile at $t = 2$ for the highest resolution simulation is shown as well. To appreciate the scale, the density ranges between $[1.0001473, 0.9998174]$. The density variation obtained suggests that the stationary equilibrium configuration, which is typified by two specific radii where

derivatives behave discontinuously, may well be subject to a higher m -mode instability, with a variation in azimuth angle $\propto m\varphi$, and indeed the longer term evolution eventually deviates from the initial setup. A rigorous stability analysis of the 1D rotating equilibrium confirms that the equilibrium is liable to a number of unstable linear eigenmodes, with e.g. a global overstable $m = 2$ mode. It is pointed out here that many of the published results obtained with SPH variants report a lesser degree of convergence, and ignore the fact that the setup may be intrinsically unstable, casting doubt on quantifying errors at even later times than those used here.

2.3.2. Kármán vortex streets

A final HD test problem adds viscous source terms to the momentum and energy equations, where we intend to simulate viscous, time-dependent flow about a cylindrical obstacle. We coded up viscosity terms corresponding to

$$\partial_t(\rho\mathbf{v}) = -\nabla \cdot (\nu\hat{\Pi}), \quad (7)$$

$$\partial_t E = -\nabla \cdot (\mathbf{v} \cdot \nu\hat{\Pi}), \quad (8)$$

where we introduce the traceless part of the kinetic pressure dyad through

$$\hat{\Pi} = -((\nabla\mathbf{v}) + (\nabla\mathbf{v})^T) + \frac{2}{3}\mathbf{I}(\nabla \cdot \mathbf{v}). \quad (9)$$

Note that we do treat these terms as sources, although their divergence-form would also allow one to include them in the flux definitions. As these source terms are identical for hydrodynamic and MHD applications, the viscous source terms are encoded in a module `amrvac/src/physics/mod_viscosity.t`, which is then shared between the HD and MHD systems.

For incompressible HD, where the velocity field is constrained by $\nabla \cdot \mathbf{v} = 0$, it is known from experimental observations that only the Reynolds number R_e is relevant in determining the flow properties downstream of the obstacle [49]. For a typical flow speed v_0 and lengthscale l_0 , the Reynolds number sets the viscosity coefficient ν through $R_e = v_0 l_0 / \nu$. As initial condition, we set units through $l_0 = 1$, $v_0 = 1$, and set up left-right symmetric potential flow about the cylinder, which has radius $r_0 = l_0/2$. The detailed profiles are given by

$$v_x = 1 + \frac{r_0^2}{r^2} - \frac{2x^2 r_0^2}{r^4}, \quad (10)$$

$$v_y = -\frac{2xy r_0^2}{r^4}, \quad (11)$$

$$p = p_0 + \frac{1}{2} \left(\frac{2r_0^2 \cos(2\theta)}{r^2} - \frac{r_0^4}{r^4} \right), \quad (12)$$

where $r^2 = x^2 + y^2$ along with $\cos(\theta) = x/r$. The density is uniform and $\rho = 1$ initially, while $p_0 = 1/\gamma M^2$, introducing a Mach number M when simulating this setup with the compressible HD system. To remain close to the expected behavior for incompressible flow, we set $M = 0.1$. We simulated three cases,

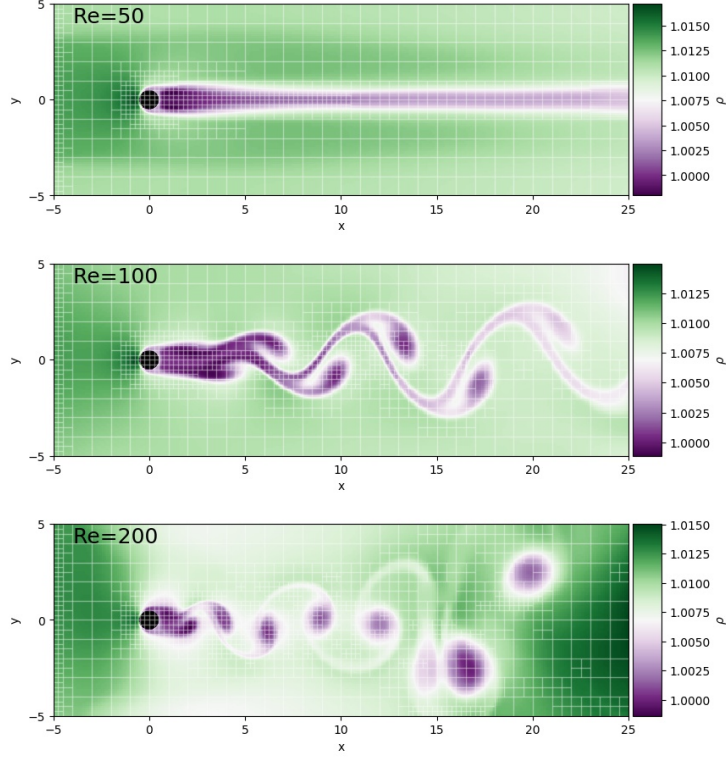


Figure 6: Compressible hydro simulations of flow about a cylinder, for fixed Mach number $M = 0.1$, at varying Reynolds number $Re = 50, 100$, to 200 . We show the density variation at $t = 85$.

which only differ in the Reynolds number Re , varied from 50 , 100 , to 200 . The left inlet boundary exploits Dirichlet boundary conditions, setting a uniform horizontal inflow corresponding to the far-field solution where $\rho = 1$, $p = p_0$ and $v_x = 1$. The other three lateral boundaries use a zero gradient extrapolation. Special to this setup is an approximate treatment of the internal region $r < 0.5$ for the cylinder: we actually nullify the full flow field within this radius, mimicking the vanishing of the flow components (in a viscous boundary layer) expected for a Navier-Stokes evolution. We further use a domain $[-5, 25] \times [-5, 5]$, employ a base level grid of 300×100 , and use AMR allowing 3 refinement levels in total. We enforce full refinement manually about the cylinder, and let the remainder of the domain regrid on the basis of variations in density and horizontal momentum ρv_x .

A strong stability preserving Runge-Kutta scheme [14], combined with an HLL flux [32] and Koren reconstruction [43] is used, and we show the obtained solutions at $t = 85$ in Fig. 6. Note that these figures show the density variation, different from the incompressible situation where the density is uniform throughout. However, we do recover the correct transition to turbulent flows, as

the Reynolds number increases, which shows how gradual symmetry breaking occurs for higher Reynolds numbers. The $R_e = 50$ solution settles on a steady state, where the original left-right symmetry of the potential flow is broken, but the up-down symmetry preserved. Higher Reynolds numbers break the up-down symmetry spontaneously, first showing fairly regular, periodic vortex shedding ($R_e = 100$), while even this transits to more chaotic behavior as R_e reaches 200. This is the typical behavior of Kármán vortex streets [49]. Our compressible simulations also show some sound wave related background variations in density induced by artificial reflections (at inlet and at the cylinder).

The same setup can also be simulated on a 2D polar AMR mesh, where the boundary conditions for vanishing flow at the cylinder radius can be enforced exactly. An impression of a $M = 0.1$, $R_e = 200$ simulation is given in Fig. 7. In this setup, the outer radial boundary treatment is less trivial (potential inflow is enforced, while open flow conditions at the right half prevail). The pressure distribution as a function of polar angle along the cylinder radius can be compared to actual flow measurements, as this setup has been studied extensively in terms of the drag coefficient. The variation of the flow properties for increasing Reynolds number can then be verified, studying e.g. vortex shedding frequencies (i.e. Strouhal number). The use of AMR helps to affordably achieve a high resolution, capturing all details in the boundary layer (such as the separation angle, possible transitions to turbulence) and the wake region.

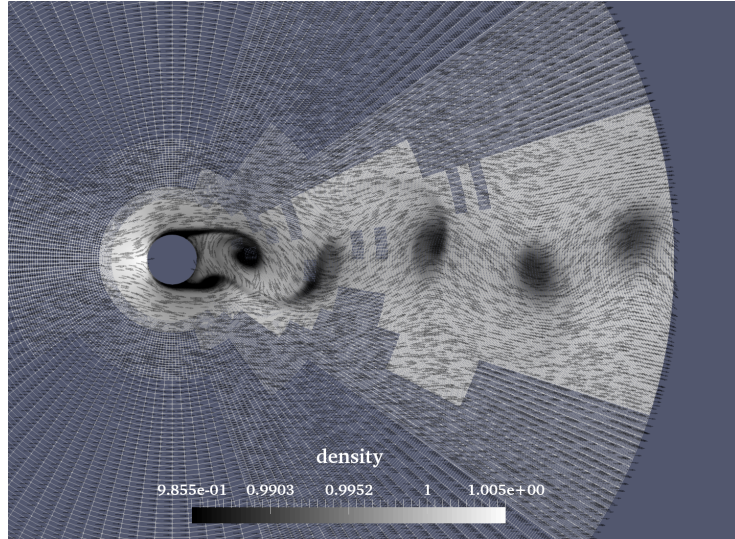


Figure 7: Compressible flow about a cylinder, computed on a polar AMR mesh, for Mach $M = 0.1$, at Reynolds number $R_e = 200$. We show the density variation at $t = 85$ in greyscale, and the flow field using arrows, along with the grid structure.

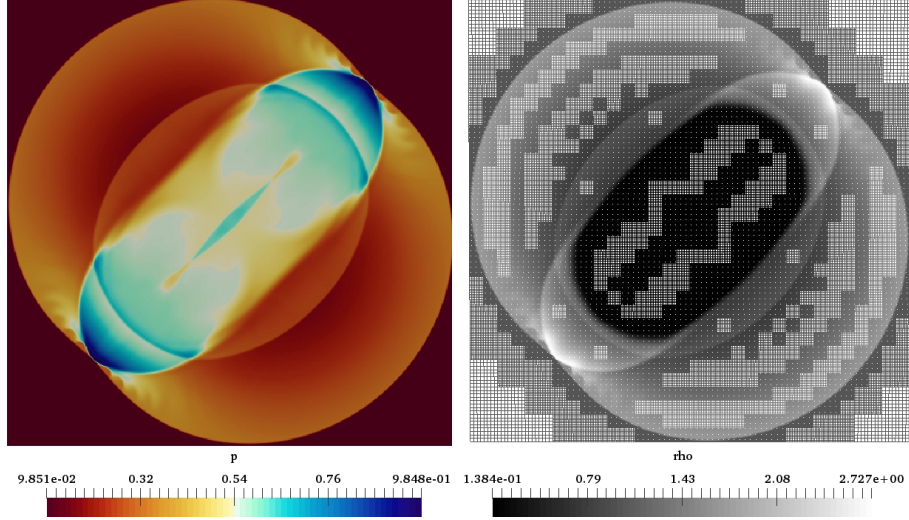


Figure 8: An MHD blast wave solution in 2D. The pressure (left) and density (right) are shown at $t = 0.2$, and an impression of the adaptive grid structure is given in the right panel.

2.4. MHD blast wave

As an example MHD run, we use a frequently quoted MHD blast wave configuration [e.g. 50, 51, 52, 53], which is in spirit similar to the circular dam break setup, but where the initially uniform magnetic field \mathbf{B} now introduces a clear anisotropy. We use the exact setup recently demonstrated in 2D in [51], where $\rho = 1$, $\gamma = 5/3$, the domain is $[-0.5, 0.5]^2$ and the magnetic field is $\mathbf{B} = (1/\sqrt{2}, 1/\sqrt{2})$. A central circular region of radius $r_{\text{blast}} = 0.1$ has an overpressure $p_{\text{in}} = 10$, in contrast to the exterior $p_{\text{ext}} = 0.1$. The plasma beta, quantifying the dimensionless ratio $\beta = 2p/B^2$ (exploiting units where the vacuum permeability $\mu_0 = 1$) ranges from 0.2 (outside) to 20 (inside the blast). The simulation is run till time $t = 0.2$.

As there is no real exact solution known, we simply show plots in a format that allows direct comparison with published 2D results. We use this setup to showcase the dimension and coordinate flexibility of our software, hence we will run it in 2D (on $[-0.5, 0.5]^2$) and 3D Cartesian (then on $[-0.5, 0.5]^3$) setups, as well as on a 2D polar and a 3D spherical grid. In [52], similar 2D and 3D results for (nearly) identical setups were shown, on both Cartesian versus polar (2D) and spherical grids (3D). [52] demonstrated the adaptation of a modern space-time conservation element and solution element (CESE) scheme on otherwise fixed, but on general curvilinear grids. This CESE scheme was also demonstrated with AMR and general curvilinear grids on MHD blast waves in [54]. In 2D polar setups, we use $r \in [1, 2]$ and $\varphi \in [-0.12\pi, 0.12\pi]$, with the initial blast at $r = 1.5$, $\varphi = 0$, as in [52]. Similarly, for the 3D Cartesian run, we set the initial field $\mathbf{B} = (1/\sqrt{3}, 1/\sqrt{3}, 1/\sqrt{3})$ to retrieve the same plasma beta regime. In the 3D spherical run, we will simulate on a shell $r \in [0.1, 1.1]$, while

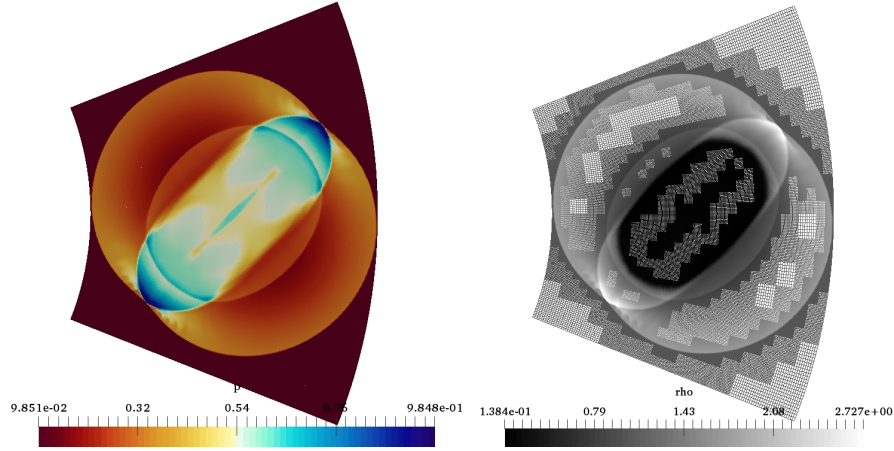


Figure 9: An MHD blast wave solution in 2D, simulated on a polar AMR grid. In the same format as Fig. 8, the pressure (left) and density (right) are shown at $t = 0.2$, and an impression of the adaptive grid structure is given in the right panel.

polar angle $\vartheta \in [0.2\pi, 0.8\pi]$ and angular variation $\varphi \in [0.7\pi, 1.3\pi]$ is used. In this spherical setup, we initialize $\mathbf{B} = (1/\sqrt{2}, 1/\sqrt{2}, 0)$, while putting the blast perturbation at $r_b = 0.6$, $\vartheta_b = \pi/2$ and $\varphi_b = \pi$. We will use AMR in all runs.

We always use a three-step time integration, an HLLC flux computation [28, 55], and the third order Cuda limiter [56] in the reconstruction. A Courant parameter of 0.9 is used, but the first 10 discrete timesteps are reduced gradually. At $t = 0.2$, the perturbation has not yet reached any lateral boundary, so the boundary conditions are fairly irrelevant: we used periodic sides in the Cartesian setups, and fixed all quantities in the polar and spherical case. The 2D runs have base resolution 64×64 , with 3 additional refinement levels hence reaching 512^2 thanks to the AMR, while the 3D runs use 64^3 , up to effective resolutions 256^3 thanks to the AMR.

In Fig. 8, the pressure (left) and density (right) are shown in contour views, where the grid structure is visible in the density panel. In this setup, the initial magnetic field is oriented along the diagonal, and the various MHD wave signals cause intricate patterns. Note in particular the pressure-density fluctuations in the north-east and south-west disturbed regions in between the outermost (fast) shock front and the more elliptical shaped signal (outlined by the blueish color in the pressure view). When repeating the simulation on a polar grid, shown in Fig. 9, the same details emerge, although in that case, the south-west part is slightly more resolved than the north-east perturbation, due to the natural r -dependence in the polar grid structure. Our Fig. 8 compares favorably with the results shown in [51], who computed on a fixed grid, using a novel fourth-order finite volume method using a constrained transport approach for handling $\nabla \cdot \mathbf{B} = 0$. Our AMR run from Fig. 9 shows more details than the polar result in [52], due to its higher effective resolution.

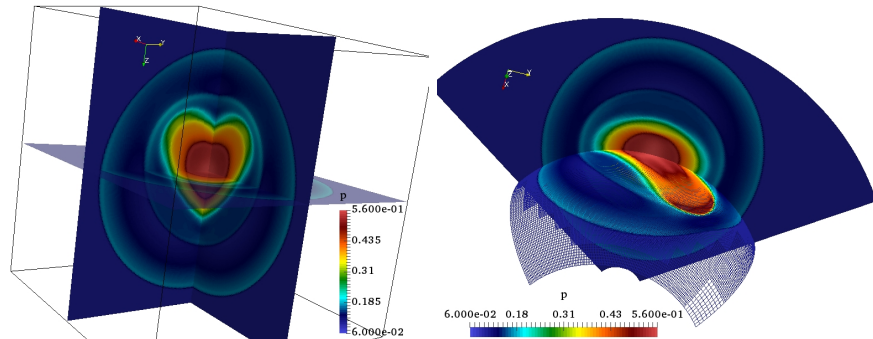


Figure 10: An MHD blast wave solution in 3D. On a Cartesian grid (left), showing the pressure on three orthogonal cutting planes (with the $z = 0$ one made translucent). On a block-AMR spherical grid (right).

We emphasize that our simulation does not exploit any staggering (all quantities are defined cell-centered), and on both the 2D and the 3D Cartesian grid, we used the multigrid functionality to control $\nabla \cdot \mathbf{B} = 0$ as described in [13]. This in practice implies the multigrid based solution of a Poisson problem $\nabla^2 \phi = \nabla \cdot \mathbf{B}^*$ where \mathbf{B}^* is the magnetic field after a (sub)step of any scheme applied, to correct it to a solenoidal $\mathbf{B} = \mathbf{B}^* - \nabla \phi$. As our multigrid solver can not handle the grid variation from a polar or spherical mesh, the way to control magnetic monopole errors in those runs was using the diffusive treatment introduced in [15], only applied to the induction equation.

The 3D simulation on the Cartesian grid is shown at left in Fig. 10, where we show the instantaneous pressure distribution on 3 cutting planes ($x = 0$, $y = 0$ and $z = 0$). Note that there are (expected) notable differences between the purely 2D and the 3D blast evolution, as recovering the 2D result would require a cylindrical, instead of a spherical, initial blast region. The final blast wave demonstration is the spherical 3D simulation, shown at right in Fig. 10. We again show the pressure distribution, shown on two surfaces ($r = 0.6$ which also gives an impression of the mesh, and $\vartheta = \pi/2$). The results compare favorably with similar 3D tests in [52].

2.5. Reaction-Diffusion models

Although the last **A** in **MPI-AMRVAC** stands for *advection*, the code can also handle problems without advection. The reaction-diffusion **amrvac/src/rd** module, which has recently been added to **MPI-AMRVAC**, can be used to solve equations with two chemical concentrations⁶. Such systems can exhibit a wide variety of pattern-forming behavior [57], as was first pointed out by Turing [58]. We specifically consider two types of models, the first being the Gray-Scott

⁶It can trivially be extended to more than two chemical species.

model	reactions	$h = 1/128$	$1/256$	$1/512$
Gray-Scott	~ 1	0.76	0.19	0.048
Schnakenberg	$\sim 10^{-2}$	1.5×10^{-5}	3.8×10^{-6}	0.95×10^{-6}

Table 1: Restriction on Δt due to reactions (first column) and due to handling diffusion explicitly for a 2D problem with grid spacing h .

model [59], which in dimensionless units has the following form

$$\begin{aligned}\partial_t u &= D_u \nabla^2 u - uv^2 + F(1 - u), \\ \partial_t v &= D_v \nabla^2 v + uv^2 - (F + k)v,\end{aligned}\tag{13}$$

where F and k are positive constants, and the diffusion coefficients are here set to $D_u = 2 \times 10^{-5}$ and $D_v = 10^{-5}$. Note that u is converted to v , and that the ‘feed’ term $F(1 - u)$ drives the concentration of u to one, whereas the term $-(F + k)v$ removes v from the system. Depending on the values of F and k , a wide range of patterns can be generated, as demonstrated in [60]. Here we use $F = 0.046$ and $k = 0.063$.

The second type of model we consider is due to Schnakenberg [61]

$$\partial_t u = D_u \nabla^2 u + \kappa(a - u + u^2 v),\tag{14}$$

$$\partial_t v = D_v \nabla^2 v + \kappa(b - u^2 v),\tag{15}$$

where κ , a and b are positive constants. The reaction terms somewhat differ from the Gray-Scott model, but the most important difference is that we will use much larger diffusion coefficients: $D_u = 0.05$, $D_v = 1$. These and other parameters ($\kappa = 100$, $a = 0.1305$ and $b = 0.7695$) are taken from [62] (Chapter IV, section 4.4).

2.5.1. Numerical implementation

The implementation of these reaction-diffusion models in **MPI-AMRVAC** is handled via source terms, using the `phys_add_source` interface. A standard second-order accurate discretization of the diffusive terms is employed, and fluxes are not considered in this module. The reaction terms are always handled explicitly, but for the diffusion terms we have implemented several options. The first is to handle diffusion explicitly, which leads to a time step restriction $\Delta t < h^2/(2N_{\text{dim}}D_{\text{max}})$, where h is the grid spacing, N_{dim} is the problem dimension and $D_{\text{max}} = \max(D_u, D_v)$ the maximum of the diffusion coefficients. Explicit time step restrictions for the reaction and diffusion terms are tabulated in Table 1. The large diffusion coefficients make the Schnakenberg model numerically stiff, even on relatively coarse grids.

A detailed comparison of numerical methods to handle stiff reaction-diffusion problems can be found in [62, 63]. In **MPI-AMRVAC**, we have implemented two schemes. The first is a simple operator splitting method. The idea is to split the time derivative as

$$\partial_t w = F(w) = F_0(w) + F_1(w),\tag{16}$$

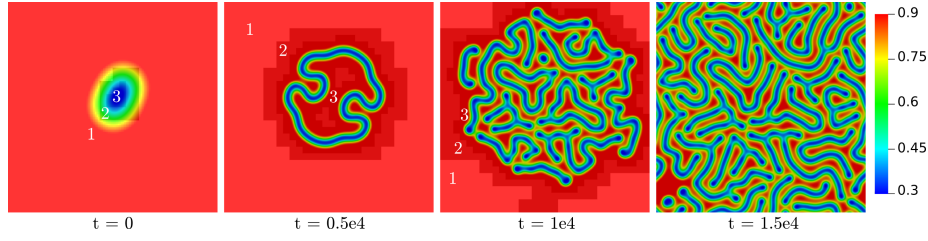


Figure 11: Time evolution of the density u in a Gray-Scott model with $F = 0.046$ and $k = 0.063$, see equation (13). Three refinement levels are used, indicated by the white number and the gray shade. The levels correspond to an effective resolution of 128^2 , 256^2 and 512^2 cells. In the rightmost picture, the whole grid is at the highest refinement level.

where F_0 are the non-stiff reaction terms and F_1 the stiff diffusion terms. The effect of F_0 can be handled explicitly to obtain w_{n+1}^* from a past state w_n , after which an implicit equation is solved to obtain the next state w_{n+1} . We use a backward-Euler discretization $w_{n+1} = w_{n+1}^* + \Delta t F_1(w_{n+1})$, which leads to a Helmholtz equation:

$$\nabla^2 w_{n+1} - \frac{1}{\Delta t D} w_{n+1} = -\frac{1}{\Delta t D} w_{n+1}^*. \quad (17)$$

This equation is solved with the parallel and AMR-compatible geometric multigrid solver that has recently been added to **MPI-AMRVAC** [13]. Such a multigrid method leads to a linear cost in the number of unknowns.

The second scheme we have implemented is the second-order accurate IMEX scheme given in [62] (eq. 4.12 of chapter IV), which is a combination of the implicit and explicit trapezoidal rule:

$$w_{n+1}^* = w_n + \Delta t F_0(w_n) + \frac{1}{2} \Delta t [F_1(w_n) + F_1(w_{n+1}^*)] \quad (18)$$

$$w_{n+1} = w_n + \frac{1}{2} \Delta t [F(w_n) + F(w_{n+1}^*)]. \quad (19)$$

When written out, the first equation again corresponds to a Helmholtz equation that can be solved with the multigrid solver.

2.5.2. Examples

Figure 11 shows the time evolution of a Gray-Scott model for which $F = 0.046$ and $k = 0.063$. The model is solved up to $t = 1.5 \times 10^4$ in a periodic 2D domain of size $L \times L$, with $L = 2$. An AMR mesh with three levels is used, corresponding to grids of 128^2 up to 512^2 cells, and the size of individual grid blocks is set to 8^2 cells. Time integration is performed with the midpoint method using a time step $\Delta t = 0.5$. The initial condition is the steady state $u = 1$ and $v = 0$ modified by two Gaussian perturbations of the form $\frac{1}{2} \exp(-25|\vec{r} - \vec{r}_i|^2)$, with $\vec{r}_1 = (0.5, 0.5)$ and $\vec{r}_2 = (0.55, 0.6)$. These perturbations are subtracted from u and added to v . A complex maze-like pattern emerges. For other values

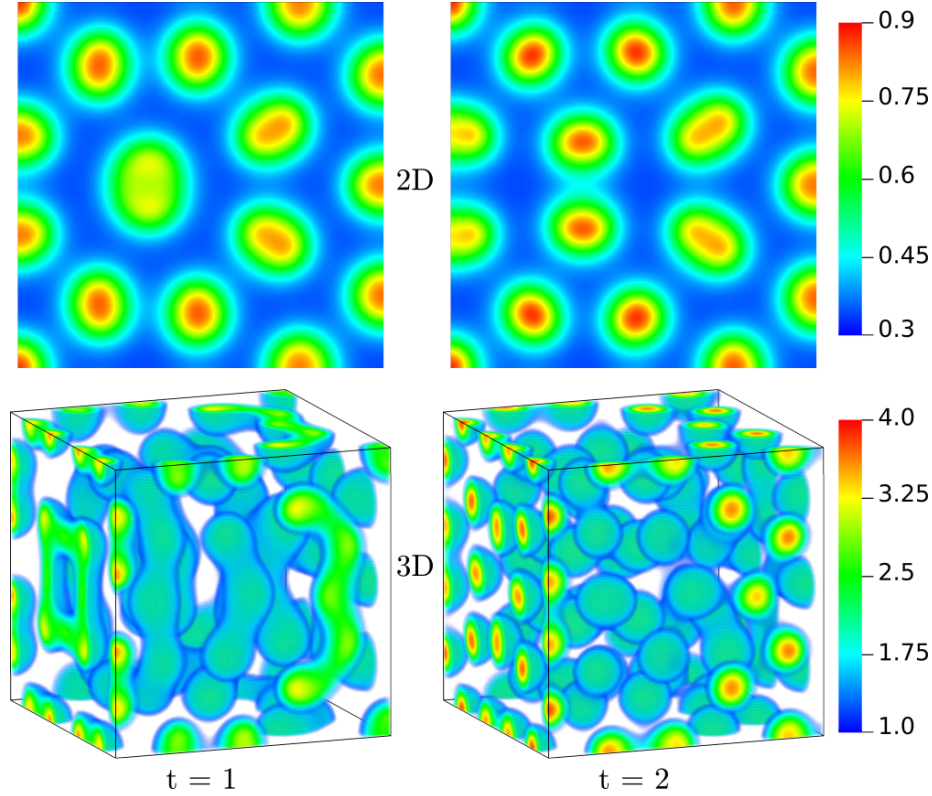


Figure 12: Time evolution of the density u in Schnakenberg's model, see equation (14). Top row: 2D case on a 256^2 uniform grid, bottom row: 3D case on a 128^3 uniform grid.

of F and k , many other types of patterns can emerge, see [60]⁷.

The evolution in figure 11 is somewhat chaotic and therefore sensitive to small numerical errors. To compare the numerical properties of reaction-diffusion schemes, we consider a 2D and 3D example in which we solve Schnakenberg's model, which has a less chaotic time evolution. Solution examples are shown in figure 12, both for 2D and 3D cases. As in [62], we use a domain with sides of length $L = 1$, and Neumann zero boundary conditions for the species densities. The initial condition is $v = b/(a + b)^2$ and $u(\vec{r}) = a + b + \exp(-100|\vec{r} - \vec{r}_0|^2)$, where $\vec{r}_0 = (1/3, 1/2)$ in 2D and $\vec{r}_0 = (1/3, 1/2, 1/2)$ in 3D.

Figure 13 shows the convergence behavior of the IMEX and the split scheme for Schnakenberg's problem in 2D solved on a uniform grid of 256^2 cells. The solution at $t = 2$ is compared to a solution computed with an explicit third-order scheme and a small time step $\Delta t = 3 \times 10^{-6}$. The IMEX scheme (from Eq. (19))

⁷Interested readers can also interactively explore such patterns at <https://mrob.com/pub/comp/xmorphism/ogl/index.html>

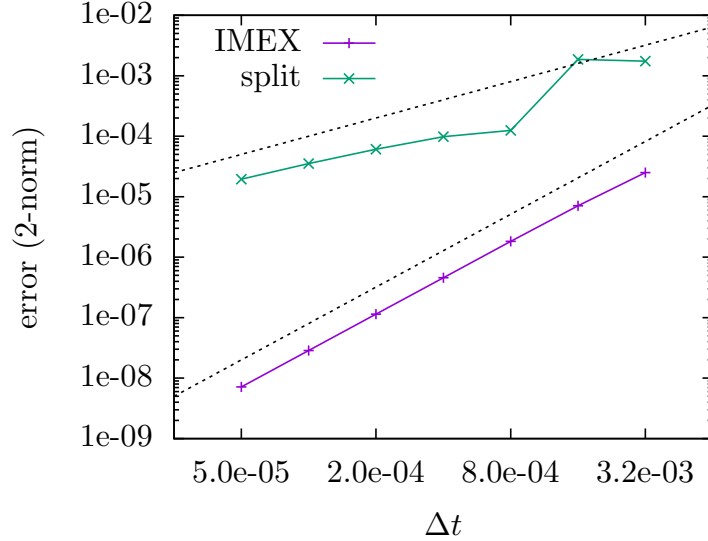


Figure 13: Time integration error (two-norm) of an IMEX and a split scheme for solving Schnakenberg’s model on a 256^2 uniform grid. The solution at $t = 2$ is compared to a solution computed with a small time step. The dashed lines indicate first and second order convergence.

performs well and exhibits second order convergence. The split scheme converges more slowly, with slightly less than first order convergence, which indicates that there are large splitting errors. These results are in agreement with [62].

To compare the computational costs of the schemes in **MPI-AMRVAC**, we ran the 256^2 test case using 4 cores of an AMD 2700X CPU. Per time step, each scheme took: explicit 1.1 ms, IMEX 7.7 ms and split 7.2 ms. For the latter two schemes, the multigrid solver consumed about 90% of the CPU time. This percentage is so high because the reaction terms are computationally cheap to evaluate. For the multigrid solver, iterations were performed until the maximum residual was less than 10^{-7} times the right-hand side of equation (17). The explicit scheme is the cheapest per time step, but it requires orders of magnitude more steps than the other methods for stability.

3. Conclusions and outlook

We gave an overview of currently available PDE systems in the open-source software **MPI-AMRVAC**, demonstrating its versatility in dimensionality, but also in the type of PDE systems to be solved. For the (M)HD system, to which it was originally targeted, various conservative, shock-capturing discretizations are implemented. With minimal effort, any near-conservative system may be implemented as a new physics module, and the framework offers a dimension-independent, parallelized means for performing high-resolution, domain decomposed or block grid-adaptive computations. The recent coupling to a geomet-

ric multigrid solver extends its versatility to any problem where Poisson or Hemholtz type constraints arise, and this was demonstrated here for a newly added reaction-diffusion set of equations. For stiff source terms, such as particular diffusion terms in these reaction-diffusion problems, we can use our framework to compare modern variants of IMEX schemes, with standard explicit treatments. We documented here how a new PDE system is readily added to the source code, and welcome any extension of our software to explore intricate spatio-temporal behavior of nonlinear PDEs.

As illustrated on both shallow water and MHD Riemann problems, the code can handle simulations on polar, cylindrical or spherical grids, which require the handling of geometric source terms. Generic gradient, vector divergence and vector curl operations are implemented in the `amrvac/src/mod_geometry.t` module, and they can all be combined with directional stretching (e.g. demonstrated for radial directions in [8]). As stated earlier, **MPI-AMRVAC** has been used successfully to handle not only Newtonian (M)HD, but its extension to special relativistic (M)HD as well [11], where also a typical 3+1 space-time formulation leads to a system of the form (1). Advanced applications to the extreme conditions encountered in pulsar wind nebulae [64, 65] focused on such relativistic plasma behavior in Minkowski space-time. Meanwhile, code variants that can handle also non-orthogonal curvilinear coordinates, where one must distinguish between covariant and contravariant vector representations, have been developed [66, 67]. The **Black Hole Accretion Code** or **BHAC** [67] solves the covariant general relativistic MHD (GRMHD) equations in a 3+1 foliation of space time, where a flexible data structure has been introduced to handle any four-metric. A recent code comparison project [68] between the most modern software efforts to simulate GRMHD conditions as suitable in the vicinity of black holes showed that **BHAC** meets all standards of merit for guiding and interpreting contemporary astrophysical research. The **BHAC** code has recently been extended with an IMEX scheme to handle the extension to general relativistic, resistive MHD equations [69], where all covariant Maxwell equations, especially also those for electric field evolutions, enter. The IMEX scheme then treats the stiff resistive source terms, and can use a staggered representation of the GR(R)MHD variables, to ensure that magnetic monopoles only occur at machine precision [70]. The code structure and modularity, especially in its parallelization and AMR strategy, is fully shared between the **MPI-AMRVAC** and **BHAC** code efforts.

Future work can extend the code applicability to incompressible (M)HD regimes, kinematic dynamo studies where only the induction equation for the evolution of \mathbf{B} from MHD is handled, or applications involving self-gravity.

Acknowledgements

RK was supported by a joint FWO-NSFC grant G0E9619N and by his ERC Advanced Grant PROMINENT, and JT was supported by FWO postdoctoral fellowship 12Q6117N. This project has received funding from the European Research Council (ERC) under the European Unions Horizon 2020 research and

innovation programme (grant agreement No. 833251 PROMINENT ERC-ADG 2018). This research is further supported by Internal funds KU Leuven, project C14/19/089 TRACESpace. The computational resources and services used in this work were provided by the VSC (Flemish Supercomputer Center), funded by the Research Foundation Flanders (FWO) and the Flemish Government - department EWI.

References

References

- [1] A. Mignone, G. Bodo, S. Massaglia, T. Matsakos, O. Tesileanu, C. Zanni, A. Ferrari, PLUTO: A Numerical Code for Computational Astrophysics, *ApJ Supplement Series* 170 (1) (2007) 228–242. [arXiv:astro-ph/0701854](#), [doi:10.1086/513316](#).
- [2] A. Mignone, C. Zanni, P. Tzeferacos, B. van Straalen, P. Colella, G. Bodo, The PLUTO Code for Adaptive Mesh Computations in Astrophysical Fluid Dynamics, *ApJ Supplement Series* 198 (1) (2012) 7. [arXiv:1110.0740](#), [doi:10.1088/0067-0049/198/1/7](#).
- [3] B. Fryxell, K. Olson, P. Ricker, F. X. Timmes, M. Zingale, D. Q. Lamb, P. MacNeice, R. Rosner, J. W. Truran, H. Tufo, FLASH: An Adaptive Mesh Hydrodynamics Code for Modeling Astrophysical Thermonuclear Flashes, *ApJ Supplement Series* 131 (1) (2000) 273–334. [doi:10.1086/317361](#).
- [4] U. Ziegler, A three-dimensional Cartesian adaptive mesh code for compressible magnetohydrodynamics, *Computer Physics Communications* 116 (1) (1999) 65–77. [doi:10.1016/S0010-4655\(98\)00139-8](#).
- [5] U. Ziegler, The NIRVANA code: Parallel computational MHD with adaptive mesh refinement, *Computer Physics Communications* 179 (4) (2008) 227–244. [doi:10.1016/j.cpc.2008.02.017](#).
- [6] J. M. Stone, T. A. Gardiner, P. Teuben, J. F. Hawley, J. B. Simon, Athena: A New Code for Astrophysical MHD, *ApJ Supplement Series* 178 (1) (2008) 137–177. [arXiv:0804.0402](#), [doi:10.1086/588755](#).
- [7] R. Teyssier, Cosmological hydrodynamics with adaptive mesh refinement. A new high resolution code called RAMSES, *A&A* 385 (2002) 337–364. [arXiv:astro-ph/0111367](#), [doi:10.1051/0004-6361:20011817](#).
- [8] C. Xia, J. Teunissen, I. El Mellah, E. Chané, R. Keppens, MPI-AMRVAC 2.0 for Solar and Astrophysical Applications, *ApJ Supplement Series* 234 (2018) 30. [arXiv:1710.06140](#), [doi:10.3847/1538-4365/aaa6c8](#).
- [9] J. P. Goedbloed, R. Keppens, S. Poedts, *Magnetohydrodynamics of laboratory and astrophysical plasmas*, Cambridge, UK: Cambridge University Press, 2019.

- [10] A. Vande Wouwer, P. Saucez, W. Schiesser (Eds.), Adaptive method of lines, Chapman & Hall/CRC Press, 2001.
- [11] R. Keppens, Z. Meliani, A. J. van Marle, P. Delmont, A. Vlasis, B. van der Holst, Parallel, grid-adaptive approaches for relativistic hydro and magnetohydrodynamics, *Journal of Computational Physics* 231 (2012) 718–744. doi:10.1016/j.jcp.2011.01.020.
- [12] D. C. Collins, H. Xu, M. L. Norman, H. Li, S. Li, Cosmological Adaptive Mesh Refinement Magnetohydrodynamics with Enzo, *ApJ Supplement Series* 186 (2) (2010) 308–333. arXiv:0902.2594, doi:10.1088/0067-0049/186/2/308.
- [13] J. Teunissen, R. Keppens, A geometric multigrid library for quadtree/octree AMR grids coupled to MPI-AMRVAC, arXiv e-prints (2019) arXiv:1901.11370arXiv:1901.11370.
- [14] O. Porth, C. Xia, T. Hendrix, S. P. Moschou, R. Keppens, MPI-AMRVAC for Solar and Astrophysics, *ApJ Supplement Series* 214 (2014) 4. arXiv:1407.2052, doi:10.1088/0067-0049/214/1/4.
- [15] R. Keppens, M. Nool, G. Tóth, J. P. Goedbloed, Adaptive Mesh Refinement for conservative systems: multi-dimensional efficiency evaluation, *Computer Physics Communications* 153 (3) (2003) 317–339. arXiv:astro-ph/0403124, doi:10.1016/S0010-4655(03)00139-5.
- [16] M. H. J. Leroy, R. Keppens, On the influence of environmental parameters on mixing and reconnection caused by the Kelvin-Helmholtz instability at the magnetopause, *Physics of Plasmas* 24 (1) (2017) 012906. doi:10.1063/1.4974758.
- [17] E. Chané, J. Saur, R. Keppens, S. Poedts, How is the Jovian main auroral emission affected by the solar wind?, *Journal of Geophysical Research (Space Physics)* 122 (2) (2017) 1960–1978. doi:10.1002/2016JA023318.
- [18] W. Ruan, C. Xia, R. Keppens, Extreme-ultraviolet and X-Ray Emission of Turbulent Solar Flare Loops, *ApJ Letters* 877 (1) (2019) L11. doi:10.3847/2041-8213/ab1f78.
- [19] Y.-H. Zhou, C. Xia, R. Keppens, C. Fang, P. F. Chen, Three-dimensional MHD Simulations of Solar Prominence Oscillations in a Magnetic Flux Rope, *ApJ* 856 (2) (2018) 179. arXiv:1803.03385, doi:10.3847/1538-4357/aab614.
- [20] C. Xia, R. Keppens, X. Fang, Coronal rain in magnetic bipolar weak fields, *A&A* 603 (2017) A42. arXiv:1706.01804, doi:10.1051/0004-6361/201730660.

- [21] I. El Mellah, A. A. C. Sander, J. O. Sundqvist, R. Keppens, Formation of wind-captured disks in supergiant X-ray binaries. Consequences for Vela X-1 and Cygnus X-1, *A& A* 622 (2019) A189. doi:10.1051/0004-6361/201834498.
- [22] G. Tóth, A General Code for Modeling MHD Flows on Parallel Computers: Versatile Advection Code, *Astrophysical Letters and Communications* 34 (1996) 245.
- [23] G. Tóth, D. Odstrčil, Comparison of Some Flux Corrected Transport and Total Variation Diminishing Numerical Schemes for Hydrodynamic and Magnetohydrodynamic Problems, *Journal of Computational Physics* 128 (1) (1996) 82–100. doi:10.1006/jcph.1996.0197.
- [24] R. Keppens, G. Tóth, M. A. Botchev, A. van der Ploeg, Implicit and semi-implicit schemes: Algorithms, *International Journal for Numerical Methods in Fluids* 30 (3) (1999) 335–352. doi:10.1002/(SICI)1097-0363(19990615)30:3<335::AID-FLD923>3.3.CO;2-L.
- [25] R. Keppens, G. Tóth, Nonlinear dynamics of Kelvin-Helmholtz unstable magnetized jets: Three-dimensional effects, *Physics of Plasmas* 6 (5) (1999) 1461–1469. arXiv:astro-ph/9901383, doi:10.1063/1.873398.
- [26] R. Keppens, G. Tóth, R. H. J. Westermann, J. P. Goedbloed, Growth and saturation of the Kelvin-Helmholtz instability with parallel and antiparallel magnetic fields, *Journal of Plasma Physics* 61 (1) (1999) 1–19. arXiv:astro-ph/9901166, doi:10.1017/S0022377898007223.
- [27] G. Tóth, The $\nabla \cdot \mathbf{B} = 0$ Constraint in Shock-Capturing Magnetohydrodynamics Codes, *Journal of Computational Physics* 161 (2) (2000) 605–652. doi:10.1006/jcph.2000.6519.
- [28] E. Toro, *Riemann solvers and Numerical methods for Fluid dynamics*, Berlin, Springer-Verlag, 1997.
- [29] R. J. Leveque, *Finite volume methods for hyperbolic problems*, Cambridge, UK: Cambridge University Press, 2002.
- [30] B. van der Holst, R. Keppens, Z. Meliani, A multidimensional grid-adaptive relativistic magnetofluid code, *Computer Physics Communications* 179 (9) (2008) 617–627. arXiv:0807.0713, doi:10.1016/j.cpc.2008.05.005.
- [31] V. Rusanov, The calculation of the interaction of non-stationary shock waves and obstacles, *USSR Comp. Math. and Math. Phys.* 1 (1961) 304–320.
- [32] A. Harten, P. Lax, B. van Leer, On upstream differencing and Godunov-type schemes for hyperbolic conservation laws, *SIAM Rev.* 25 (1983) 35–61.

- [33] G. Tóth, The LASX Preprocessor and Its Application to General Multi-dimensional Codes, *Journal of Computational Physics* 138 (2) (1997) 981–990. doi:10.1006/jcph.1997.5813.
- [34] R. Lohner, An adaptive finite element scheme for transient problems in CFD, *Computer Methods in Applied Mechanics and Engineering* 61 (3) (1987) 323–338. doi:10.1016/0045-7825(87)90098-3.
- [35] R. Keppens, O. Porth, Scalar hyperbolic PDE simulations and coupling strategies, *J. Comput. and Applied Math.* 266 (2014) 87–101.
- [36] N. J. Zabusky, M. D. Kruskal, Interaction of “Solitons” in a Collisionless Plasma and the Recurrence of Initial States, *Phys. Rev. Lett.* 15 (6) (1965) 240–243. doi:10.1103/PhysRevLett.15.240.
- [37] C.-T. Lee, J.-E. Lin, C.-C. Lee, M.-L. Liu, Some remarks on the stability condition of numerical scheme of the KdV-type equation, *Journal of Mathematics Research* 9. doi:10.5539/jmr.v9n4p11.
- [38] A. I. Delis, T. Katsaounis, Numerical solution of the two-dimensional shallow water equations by the application of relaxation methods, *Applied Mathematical Modelling* 29 (2005) 754–783. doi:10.1016/j.apm.2004.11.001.
- [39] C. Zoppou, S. Roberts, Numerical solution of the two-dimensional unsteady dam break, *Applied Mathematical Modelling* 24 (2000) 457–475.
- [40] T. Hendrix, R. Keppens, A. J. van Marle, P. Camps, M. Baes, Z. Meliani, Pinwheels in the sky, with dust: 3D modelling of the Wolf-Rayet 98a environment, *MNRAS* 460 (4) (2016) 3975–3991. arXiv:1605.09239, doi:10.1093/mnras/stw1289.
- [41] E. Toro, *Shock-capturing methods for free-surface shallow flows*, Wiley, New York, 2001.
- [42] B. van der Holst, R. Keppens, Hybrid block-AMR in cartesian and curvilinear coordinates: MHD applications, *Journal of Computational Physics* 226 (1) (2007) 925–946. doi:10.1016/j.jcp.2007.05.007.
- [43] B. Koren, *Numerical methods for advection–diffusion problems*, Vieweg, Braunschweig, 1993.
- [44] P. Chang, J. Wadsley, T. R. Quinn, A moving-mesh hydrodynamic solver for ChaNGa, *MNRAS* 471 (3) (2017) 3577–3589. arXiv:1707.05333, doi:10.1093/mnras/stx1809.
- [45] J. W. Wadsley, B. W. Keller, T. R. Quinn, Gasoline2: a modern smoothed particle hydrodynamics code, *MNRAS* 471 (2) (2017) 2357–2369. arXiv:1707.03824, doi:10.1093/mnras/stx1643.

- [46] P. Mocz, M. Vogelsberger, D. Sijacki, R. Pakmor, L. Hernquist, A discontinuous Galerkin method for solving the fluid and magnetohydrodynamic equations in astrophysical simulations, *MNRAS* 437 (1) (2014) 397–414. [arXiv:1305.5536](#), [doi:10.1093/mnras/stt1890](#).
- [47] P. F. Hopkins, A new class of accurate, mesh-free hydrodynamic simulation methods, *MNRAS* 450 (1) (2015) 53–110. [arXiv:1409.7395](#), [doi:10.1093/mnras/stv195](#).
- [48] P. M. Gresho, S. T. Chan, On the theory of semi-implicit projection methods for viscous incompressible flow and its implementation via a finite element method that also introduces a nearly consistent mass matrix. II - Implementation, *International Journal for Numerical Methods in Fluids* 11 (1990) 621–659. [doi:10.1002/flid.1650110510](#).
- [49] U. Frisch, *Turbulence*, Cambridge, UK: Cambridge University Press, 1995.
- [50] D. S. Balsara, M. Dumbser, Divergence-free MHD on unstructured meshes using high order finite volume schemes based on multidimensional Riemann solvers, *Journal of Computational Physics* 299 (2015) 687–715. [doi:10.1016/j.jcp.2015.07.012](#).
- [51] K. G. Felker, J. M. Stone, A fourth-order accurate finite volume method for ideal MHD via upwind constrained transport, *Journal of Computational Physics* 375 (2018) 1365–1400. [arXiv:1711.07439](#), [doi:10.1016/j.jcp.2018.08.025](#).
- [52] Y. Yang, X.-S. Feng, C.-W. Jiang, An upwind CESE scheme for 2D and 3D MHD numerical simulation in general curvilinear coordinates, *Journal of Computational Physics* 371 (2018) 850–869. [doi:10.1016/j.jcp.2018.05.014](#).
- [53] T. A. Gardiner, J. M. Stone, An unsplit Godunov method for ideal MHD via constrained transport in three dimensions, *Journal of Computational Physics* 227 (8) (2008) 4123–4141. [arXiv:0712.2634](#), [doi:10.1016/j.jcp.2007.12.017](#).
- [54] C. Jiang, X. Feng, J. Zhang, D. Zhong, AMR Simulations of Magnetohydrodynamic Problems by the CESE Method in Curvilinear Coordinates, *Solar Physics* 267 (2) (2010) 463–491. [doi:10.1007/s11207-010-9649-6](#).
- [55] S. Li, An HLLC Riemann solver for magneto-hydrodynamics, *Journal of Computational Physics* 203 (1) (2005) 344–357. [doi:10.1016/j.jcp.2004.08.020](#).
- [56] M. Čada, M. Torrilhon, Compact third-order limiter functions for finite volume methods, *Journal of Computational Physics* 228 (11) (2009) 4118–4145. [doi:10.1016/j.jcp.2009.02.020](#).

- [57] S. Kondo, T. Miura, Reaction-diffusion model as a framework for understanding biological pattern formation, *Science* 329 (5999) (2010) 16161620. doi:10.1126/science.1179047. URL <http://dx.doi.org/10.1126/science.1179047>
- [58] A. M. Turing, The chemical basis of morphogenesis, *Bulletin of Mathematical Biology* 52 (1-2) (1990) 153197. doi:10.1007/bf02459572. URL <http://dx.doi.org/10.1007/BF02459572>
- [59] P. Gray, S. Scott, Autocatalytic reactions in the isothermal, continuous stirred tank reactor, *Chemical Engineering Science* 38 (1) (1983) 2943. doi:10.1016/0009-2509(83)80132-8. URL [http://dx.doi.org/10.1016/0009-2509\(83\)80132-8](http://dx.doi.org/10.1016/0009-2509(83)80132-8)
- [60] J. E. Pearson, Complex patterns in a simple system, *Science* 261 (5118) (1993) 189192. doi:10.1126/science.261.5118.189. URL <http://dx.doi.org/10.1126/science.261.5118.189>
- [61] J. Schnakenberg, Simple chemical reaction systems with limit cycle behaviour, *Journal of theoretical biology* 81 (3) (1979) 389–400.
- [62] W. Hundsdorfer, J. G. Verwer, Numerical solution of time-dependent advection-diffusion-reaction equations, Vol. 33, Springer Science & Business Media, 2013.
- [63] S. J. Ruuth, Implicit-explicit methods for reaction-diffusion problems in pattern formation, *Journal of Mathematical Biology* 34 (2) (1995) 148176. doi:10.1007/bf00178771. URL <http://dx.doi.org/10.1007/BF00178771>
- [64] O. Porth, S. S. Komissarov, R. Keppens, Three-dimensional magnetohydrodynamic simulations of the Crab nebula, *MNRAS* 438 (1) (2014) 278–306. arXiv:1310.2531, doi:10.1093/mnras/stt2176.
- [65] O. Porth, S. S. Komissarov, R. Keppens, Rayleigh-Taylor instability in magnetohydrodynamic simulations of the Crab nebula, *MNRAS* 443 (1) (2014) 547–558. arXiv:1405.4029, doi:10.1093/mnras/stu1082.
- [66] Z. Meliani, P. Grandclément, F. Casse, F. H. Vincent, O. Straub, F. Dauvergne, GR-AMRVAC code applications: accretion onto compact objects, boson stars versus black holes, *Classical and Quantum Gravity* 33 (15) (2016) 155010. doi:10.1088/0264-9381/33/15/155010.
- [67] O. Porth, H. Olivares, Y. Mizuno, Z. Younsi, L. Rezzolla, M. Moscibrodzka, H. Falcke, M. Kramer, The black hole accretion code, *Computational Astrophysics and Cosmology* 4 (1) (2017) 1. arXiv:1611.09720, doi:10.1186/s40668-017-0020-2.

- [68] O. Porth, K. Chatterjee, R. Narayan, C. F. Gammie, Y. Mizuno, P. Anninos, J. G. Baker, M. Bugli, C.-k. Chan, J. Davelaar, L. Del Zanna, Z. B. Etienne, P. C. Fragile, B. J. Kelly, M. Liska, S. Markoff, J. C. McKinney, B. Mishra, S. C. Noble, H. Olivares, B. Prather, L. Rezzolla, B. R. Ryan, J. M. Stone, N. Tomei, C. J. White, Z. Younsi, K. Akiyama, A. Alberdi, W. Alef, K. Asada, R. Azulay, A.-K. Bacsko, D. Ball, M. Baloković, J. Barrett, D. Bintley, L. Blackburn, W. Boland, K. L. Bouman, G. C. Bower, M. Bremer, C. D. Brinkerink, R. Brissenden, S. Britzen, A. E. Broderick, D. Brogiere, T. Bronzwaer, D.-Y. Byun, J. E. Carlstrom, A. Chael, S. Chatterjee, M.-T. Chen, Y. Chen, I. Cho, P. Christian, J. E. Conway, J. M. Cordes, Geoffrey, B. Crew, Y. Cui, M. De Laurentis, R. Deane, J. Dempsey, G. Desvignes, S. S. Doeleman, R. P. Eatough, H. Falcke, V. L. Fish, E. Fomalont, R. Fraga-Encinas, B. Freeman, P. Friberg, C. M. Fromm, J. L. Gómez, P. Galison, R. García, O. Gentaz, B. Georgiev, C. Goddi, R. Gold, M. Gu, M. Gurwell, K. Hada, M. H. Hecht, R. Hesper, L. C. Ho, P. Ho, M. Honma, C.-W. L. Huang, L. Huang, D. H. Hughes, S. Ikeda, M. Inoue, S. Issaoun, D. J. James, B. T. Jannuzi, M. Janssen, B. Jeter, W. Jiang, M. D. Johnson, S. Jorstad, T. Jung, M. Karami, R. Karuppusamy, T. Kawashima, G. K. Keating, M. Kettinis, J.-Y. Kim, J. Kim, J. Kim, M. Kino, J. Y. Koay, Patrick, M. Koch, S. Koyama, M. Kramer, C. Kramer, T. P. Krichbaum, C.-Y. Kuo, T. R. Lauer, S.-S. Lee, Y.-R. Li, Z. Li, M. Lindqvist, K. Liu, E. Liuzzo, W.-P. Lo, A. P. Lobanov, L. Loinard, C. Lonsdale, R.-S. Lu, N. R. MacDonald, J. Mao, D. P. Marrone, A. P. Marscher, I. Martí-Vidal, S. Matsushita, L. D. Matthews, L. Medeiros, K. M. Menten, I. Mizuno, J. M. Moran, K. Moriyama, M. Moscibrodzka, C. Müller, H. Nagai, N. M. Nagar, M. Nakamura, G. Narayanan, I. Natarajan, R. Neri, C. Ni, A. Noutsos, H. Okino, T. Oyama, F. Özel, D. C. M. Palumbo, N. Patel, U.-L. Pen, D. W. Pesce, V. Piétu, R. Plambeck, A. PopStefanija, J. A. Preciado-López, D. Psaltis, H.-Y. Pu, V. Ramakrishnan, R. Rao, M. G. Rawlings, A. W. Raymond, B. Ripperda, F. Roelofs, A. Rogers, E. Ros, M. Rose, A. Roshaninshat, H. Rottmann, A. L. Roy, C. Ruszczyk, K. L. J. Rygl, S. Sánchez, D. Sánchez-Arguelles, M. Sasada, T. Savolainen, F. P. Schloerb, K.-F. Schuster, L. Shao, Z. Shen, D. Small, B. W. Sohn, J. SooHoo, F. Tazaki, P. Tiede, R. P. J. Tilanus, M. Titus, K. Toma, P. Torne, T. Trent, S. Trippe, S. Tsuda, I. van Bemmelen, H. J. van Langevelde, D. R. van Rossum, J. Wagner, J. Wardle, J. Weintraub, N. Wex, R. Wharton, M. Wielgus, G. N. Wong, Q. Wu, K. Young, A. Young, F. Yuan, Y.-F. Yuan, J. A. Zensus, G. Zhao, S.-S. Zhao, Z. Zhu, (The Event Horizon Telescope Collaboration, The Event Horizon General Relativistic Magnetohydrodynamic Code Comparison Project, *The Astrophysical Journal Supplement Series* 243 (2) (2019) 26. [arXiv:1904.04923](#), [doi:10.3847/1538-4365/ab29fd](#).
- [69] B. Ripperda, F. Bacchini, O. Porth, E. R. Most, H. Olivares, A. Nathanail, L. Rezzolla, J. Teunissen, R. Keppens, General relativistic resistive magnetohydrodynamics with robust primitive variable recovery for accretion disk

simulations, arXiv e-prints (2019) [arXiv:1907.07197](#)[arXiv:1907.07197](#).

- [70] H. Olivares, O. Porth, J. Davelaar, E. R. Most, C. M. Fromm, Y. Mizuno, Z. Younsi, L. Rezzolla, Constrained transport and adaptive mesh refinement in the Black Hole Accretion Code, arXiv e-prints (2019) [arXiv:1906.10795](#)[arXiv:1906.10795](#).